High-speed photothermal off-resonance atomic force microscopy reveals assembly routes of centriolar scaffold protein SAS-6

Adrian P. Nievergelt[1], Niccolò Banterle[2], Santiago H. Andany[1], Pierre Gönczy[2] and Georg E. Fantner[1*]

[1]Laboratory for Bio- and Nano-Instrumentation, Swiss Federal Institute of Technology Lausanne (EPFL), Lausanne 1015, Switzerland.

[2]Swiss Institute for Experimental Cancer Research (ISREC), School of Life Sciences, Swiss Federal Institute of Technology Lausanne (EPFL), Lausanne 1015, Switzerland.

[*]Corresponding author email georg.fantner@epfl.ch

Self-assembly of protein complexes is at the core of many fundamental biological processes[1], ranging from polymerization of cytoskeletal elements such as microtubules[2], to viral capsid formation and organelle assembly[3]. To reach a comprehensive understanding of the underlying mechanisms of self-assembly, high spatial and temporal resolution must be attained. This is complicated by the need to not interfere with the reaction during the measurement. Since self-assemblies are often governed by weak interactions, they are especially difficult to monitor with high-speed atomic force microscopy due to non-negligible tip-sample interaction forces involved in current methods. Here, we develop a high-speed atomic force microscopy technique, photothermal off-resonance tapping (PORT), which is gentle enough to monitor self-assembly reactions driven by weak interactions. We apply PORT to dissect the self-assembly reaction of SAS-6 proteins, which form a nine-fold radially symmetric ring-containing structure that seeds formation of the centriole organelle. Our analysis reveals the kinetics of SAS-6 ring formation and demonstrates that distinct biogenesis routes can be followed to assemble a nine-fold symmetrical structure.

Many biological structures are assembled and disassembled in a dynamic fashion to fulfil their function. Such dynamicity is often facilitated by low binding energies, as evidenced by relatively high dissociation constants (Kd), for instance of $0.8\mu M$ for the $\alpha\beta$-tubulin complex[4] or of $10\mu M$ for the HIV capsid homodimers[5]. The resulting geometry of protein assemblies, for example the length of microtubules, often depends on the corresponding assembly/disassembly kinetics. In order to a) understand the biogenesis of macromolecular structures, it is essential to observe such kinetics in real time with single-molecule resolution. High-speed atomic force microscopy in amplitude-modulation mode (HS-AM-AFM, also known as HS-tapping mode) is a powerful tool to study the dynamics of single proteins[6] or of tightly bound protein assemblies[7]. Striking examples include pioneering studies on the actin-myosin complex[6], which has a dissociation constant (Kd) of 0.5nM-10nM[8], or of bacteriorhodopsin trimers embedded in a membrane[9]. However using HS-AM-AFM to

35   analyse the assembly dynamics of weaker interactions, with dissociation constants in the µM regime

36   or above, has proven difficult.

37   A striking example of a weak interaction at the root of an important self-assembling structure

38   is that occurring between homodimers of SAS-6, a scaffold protein required for centriole assembly in

39   organisms from algae to men[10,11]. Centrioles are nine-fold radially symmetric microtubule-based

40   organelles that play critical roles in eukaryotic cell physiology[12]. Homodimers of SAS-6 proteins

41   undergo higher order oligomerization through a weak interaction mediated by their globular head

42   domain, with a dissociation constant of ~60 µM[10,11]. These higher order oligomers form 9-fold

43   symmetric ring-like structures that initiate centriole formation *in vivo*, imparting the signature nine-

44   fold radial symmetry to the entire organelle[13,14] (Fig. 1a). Recombinantly produced homodimers of the

45   *Chlamydomonas reinhardtii* SAS-6 protein truncated of its C-terminal domain (hereafter referred to

46   as CrSAS-6; Methods) can form structures containing nine-fold radially symmetrical rings also *in vitro*[10]

47   that can be observed after their assembly using TEM[10] or AFM[15,16] (Fig. 1b, Figure S5). However, the

48   dynamics of SAS-6 ring assembly have not been resolved to date, precluding a thorough understanding

49   of the mechanisms at the root of centriole biogenesis.

50   We attempted to image CrSAS-6 ring assembly dynamics with HS-AM-AFM on our home built

51   instrument described in the Methods section (Fig. 1c, d), as well as on a commercial HS-AFM (data not

52   shown). However, we found that whereas some homodimers associate to form intermediate assembly

53   states (Fig. 1c), no full rings are formed in the imaging area (Fig. 1d, dashed box and green inset,

54   supplementary video 1, Figure S2, Table S1). By contrast, we found that full ring structures had formed

55   in the regions surrounding the area that was imaged throughout the experiment (Fig. 1d, red inset,

56   magenta circles). Likewise, imaging fully assembled rings with HS-AM-AFM leads to their disruption

57   (Figure S1, Figure S3, supplementary video 2). Together, these observations suggest that the tip-

58   sample interaction during HS-AM-AFM imaging interferes with the assembly process and ring stability.

59   Force-distance curve based AFM[17] (FD-AFM, PeakForce tapping) has been used previously to observe

60   fully assembled SAS-6 rings using 45-65pN force set points[15,16]. For imaging biological samples in

61   solution, tip forces have been reported to be significantly less than in AM-AFM when using FD-AFM

62   with cycle-to-cycle feedback [18–21]. We refer to this general AFM class as off-resonance tapping (ORT),

63   to make a clear distinction with resonant modes like AM-AFM or frequency modulation (FM-AFM),

64   and to avoid confusion with existing commercial implementations of force-distance based imaging

65   modes. However, currently available ORT methods are inherently too slow to measure the dynamics

66   of self-assembly reactions like that of SAS-6 proteins. Here, we present an advanced ORT imaging

67   mode using photothermal actuation[22] referred to as photothermal off-resonance tapping (PORT),

68 which enables force distance curves up to two orders of magnitude faster than in conventional

69 methods.

70   In ORT, the achievable imaging speed is limited by the rate at which the cantilever tip can be

71 moved up and down relative to the sample in a controlled manner. In conventional ORT

72 implementations, this motion is performed by a piezo moving the cantilever chip or the sample (Fig

73 2a). Moving such a relatively large mass limits the force-curve rate to a few kHz for most scanners and

74 up to 32 kHz for advanced designs[23]. In contrast, when utilizing photothermal actuation[22] with the

75 bimorph effect in a coated cantilever, the mass that needs to be moved is comprised only of the

76 cantilever and the tip (Fig. 2b). This allows ramp speeds of several hundred kHz (Fig. 2d), limited only

77 by the resonance of the cantilever (Fig. 2c). Since the cantilever is being actuated directly, the

78 measured cantilever deflection consists of the tip-sample force interaction of interest, and a

79 background motion (Fig. 2b, inset left). The tip-sample interaction can be determined by recording

80 the background motion slightly above the surface, and subtracting it in real time from the ORT curves

81 when imaging on the actual surface (Fig. 2b, inset center, Fig. 3a, SI section 2). This background

82 corrected time trace can then be reconstructed into a tip-sample force curve (Fig. 2b, inset right).

83   To determine the minimally achievable tip-sample forces in PORT using a commercial 8x2um

84 high-speed cantilever (BioLever Fast BLAC-10DS, Olympus, k=0.22 N/m, $f_{\mathrm{res}}^{\mathrm{fluid}}$=505 kHz, Q=1.5), we

85 recorded highly averaged time traces of the tip-sample interaction at 100kHz ORT rate, and 20nm

86 amplitude in imaging buffer on freshly cleaved Mica surfaces (Methods). Neglecting viscoelastic

87 behaviour of the sample, the force exerted by the cantilever on the sample consists of two

88 components: the static force given by the cantilever deflection, and the dynamic impact force due to

89 the abrupt deceleration of the moving tip[19]. The dynamic impact force is given by Newton's law as

90 $$F_{\mathrm{dyn}} = m_{\mathrm{eff}} \cdot a$$

91 with $m_{\mathrm{eff}} = k/(2\pi f_{\mathrm{res}})^2$ being the effective mass[19] and a the acceleration of the cantilever. In

92 conventional ORT, the dynamic force can usually be neglected because of the relatively low velocity

93 of the tip at impact. As the rate, and consequently the impact velocity, increases with PORT, the impact

94 force of ~150pN (Fig. 3b) can easily exceed the static force set-point of 80pN (Fig. 3a). In the highly

95 damped case of imaging in liquid with small, soft cantilevers, the cantilever approaches critical

96 damping. Then, assuming Hertzian mechanics, the maximum impact force P^* scales with

97 $$P^* \propto \left(\frac{f_m}{f_{\mathrm{res}}}\right)^{\frac{6}{5}} \quad (1)$$

98 where f_m is the measurement frequency, and f_{res} the cantilever resonance frequency[24] (see SI section

99 5 for details and derivation). This equation does not make any assumptions about the feedback mode,

100 and is therefore also valid for AM-AFM measurements in highly damped environments.

101   To compare the tip sample forces in HS-PORT with those in HS-AM-AFM, we recorded highly

102   averaged time traces of the same cantilevers deflection when exciting at resonance and feeding back

103   on the amplitude. From this, we measured dynamic tip-sample forces of ~800pN for HS-AM-AFM (Fig.

104   3c,d), compared to ~150pN for HS-PORT (Fig. 3b). We calculated the kinetic energies of the cantilever

105   at impact for HS-AM-AFM as $2.5 \cdot 10^{-19} J$ (Fig. 3c), and for HS-PORT as $1.12 \cdot 10^{-20} J$ for a 50pN set-

106   point (Fig. 3a). Moreover, we found that the tip-sample forces in HS-AM-AFM increase rapidly with

107   increasingly aggressive set points (Fig. 3f&h), as previously established[19,21,25]. Very high set-points

108   >90% can lead to parachuting artefacts in imaging, unless specialized instrumentation is used, such as

109   gain scheduling control[26]. By contrast, the impact force in HS-PORT scales more gradually with the set-

110   point (Fig. 3e, 3i). Equation (1) suggests that the dynamic force component scales with the ratio of

111   measurement frequency to the cantilever resonance frequency. In the case of HS-AM-AFM, the

112   measurement frequency and the resonance frequency are inherently linked and practically equal,

113   whereas in HS-PORT, the measurement frequency can be chosen freely, provided it is sufficiently

114   below the first resonance of the cantilever[27]. In addition, resonance based techniques require

115   advanced electronics for single-cycle detection[28,29]. We measured the dynamic forces for different

116   ratios of measurement frequency to resonance frequency (Fig. 3g). Fitting this curve with a

117   constrained power law, we found an exponent of 1.3 (95% confidence interval 1.22-1.40). The fact

118   that the measured exponent is slightly larger than the 1.2 predicted by the estimation of the Hertzian

119   model suggests that although the latter is a good first approximation, most likely other factors play a

120   role as well. Future development of a full theoretical model for PORT, based on time dependent, non-

121   linear contact mechanics could potentially describe the influence of other factors on the dynamic

122   force, such as ORT amplitude and impact angle. However, the frequency ratio dependence already

123   provides an intuitive explanation for why the measured tip-sample forces in HS-PORT are substantially

124   lower than in HS-AM-AFM.

125   In our discussion of AM-AFM we limit ourselves to AM-AFM experiments where the amplitude of the

126   oscillation is higher than the decay lengths of the interaction forces[30]. By contrast, recent amplitude

127   modulation 3D AFM measurements[31] with very small oscillation amplitude do not suffer from this

128   effect. However, they are less suited for observing dynamic processes due to the required

129   independent z-motion overlaid on the tip oscillation.

130   Having established the advantages of PORT for gentle and rapid topological probing, we

131   proceeded to utilize this novel imaging mode to monitor the assembly of CrSAS-6 rings with a home-

132   built AFM (SI section 3,4), using a concentration of ~61nM, in the order of that estimated for the

133   homologous protein HsSAS-6 in the cytoplasm of human cells at the onset of centriole assembly[32,33].

134   As shown in Fig. 4a, in contrast to what we had observed with HS-AM-AFM (see Fig. 1c), we found

using HS-PORT that there is no noticeable difference in the number of fully formed rings when comparing the area imaged during assembly and the surrounding regions. At sufficiently high force set-points, disruption of formed rings can nevertheless be controllably induced (see Figures S1-S3). During the imaging, a manifold of distinct, highly dynamic self-assembly reactions can be observed (as exemplified in Fig. 4b, see supplemental videos 3-5). As a first step towards characterizing the dynamics of CrSAS-6 ring assembly, we set out to determine the time needed to assemble a full CrSAS-6 ring, thus estimating how quickly the process could occur *in vivo*. As shown in Fig. 4c, HS-PORT imaging revealed that CrSAS-6 rings assemble in 106s on average. The canonical route leading to ring assembly of CrSAS-6 proteins is believed to entail the sequential addition of homodimers, from the initial single homodimer to the nine homodimers present in the ring structure. Strikingly, HS-PORT imaging uncovered that whereas such an assembly route is indeed observed (Fig. 4d.i, supplemental video 6), other assembly routes exist as well. These include the merging of two higher order multimeric units (Fig. 4d.ii, supplemental video 7), and interlinked half-circle structures that undergo topological rearrangement and relaxation into a ring (Fig. 4d.iii, supplemental video 8). The existence of different assembly routes demonstrates that the SAS-6 assembly process is not deterministic, but instead somewhat plastic. Such plasticity lends itself better to regulation, including by partner proteins in the cellular context, and offers greater potential for efficient repair.

The use of photothermal actuation for off resonance tapping enabled us to probe assembly reactions governed by weak protein interactions, as exemplified in the case of SAS-6 proteins. Traditionally, photothermal actuation is used exclusively to excite cantilevers at resonance, in part because the photothermal drive efficiency is limited for normal sized cantilevers, resulting in a small achievable off-resonance actuation range. For small cantilevers such as the AC-10, however, the drive efficiency is much higher because the thickness ratio of coating to cantilever base material is more beneficial[34], thereby allowing sufficient ORT amplitudes (see Fig. 2d). The use of photothermal excitation for ORT allowed us to increase the speed by approximately two orders of magnitude using commercially available cantilevers. Because the dynamic tip-sample force decreases with increased cantilever resonance frequency, developing even smaller cantilevers will directly increase the imaging speed while decreasing the impact forces (Fig. 3g).

Factors other than the inherent tip-sample interaction force could also play a role in HS-PORT measurements being better suited than HS-AM-AFM for imaging CrSAS-6 assemblies. To obtain acceptably small forces in AM-AFM, small amplitudes should be used. However, even at amplitudes of 1-4nm and set point amplitudes of 90%, we were not able to image without impairing self-assembly (see Figure S2, Figure S4). Due to the finite speed of the feedback loop, the sample will be subjected to lateral forces upon a change in topography, even when imaging molecular structures of a few nm

169 in height. These forces act in plane with the weak self-assembly forces, and therefore directly affect

170 the dissociation probability. In PORT, the ramp amplitude can be chosen larger while still maintaining

171 acceptably small forces, because of the lower f_d/f_{res} ratio.

172 In our current implementation of HS-PORT, heating is minimized by using a pulsed operation

173 of the drive laser rather than a continuous sinusoidal actuation (see Figure S10), which more than

174 halves the average heat on the cantilever. The resulting cantilever motion is sufficiently sinusoidal on

175 the down part of the curve so that the assessment of the impact forces is still applicable. In the future,

176 optimizing the cantilever coating materials and thicknesses will further improve drive efficiency, which

177 will allow larger actuation range while reducing heating.

178 Using HS-ORT allowed us to monitor the molecular dynamics of SAS-6 assembly. Because the

179 Mica-CrSAS-6 interaction most likely influences the reaction kinetics, the measured assembly time

180 should be considered as an order of magnitude indication rather than an exact representation of the

181 *in vivo* assembly time. Nevertheless, understanding the assembly kinetics of CrSAS-6 rings *in vitro*

182 could help shed light on the conditions relevant to cartwheel assembly *in vivo*, which *occurs* exclusively

183 on surfaces[35], as is the case in the present cell-free assay. Moreover, multiple rings of SAS-6 proteins

184 stack to create the cartwheel structure *in vivo*, likely assisted by other molecular partners [35]. How

185 these molecular partners contribute to cartwheel formation is not yet understood. In the future,

186 performing HS-PORT measurements in the presence of such molecular partners will further help

187 understand this crucial self-assembly mechanism occurring in eukaryotic cells.

188

Author contributions

190 A.P.N and N.B contributed equally to this work. A.P.N Designed and built the instrument, performed

191 experiments, analysed data and wrote the paper. N.B. prepared samples, performed experiments,

192 analysed data and wrote the paper. S.H.A. built instrumentation. P.G conceived experiments and

193 wrote the paper. G.E.F designed the instruments, conceived experiments and wrote the paper. All

194 authors discussed the results and commented on the manuscript.

195

196

Additional Information

Competing financial interests

212 The authors declare no competing financial interests.

213

References

1. Kushner, D. J. Self-assembly of biological structures. *Bacteriol. Rev.* **33,** 302–345 (1969).

2. Mandelkow, E. M. Microtubule dynamics and microtubule caps: a time-resolved cryo-electron microscopy study. *J. Cell Biol.* **114,** 977–991 (1991).

3. Cameron, J. C., Wilson, S. C., Bernstein, S. L. & Kerfeld, C. A. Biogenesis of a Bacterial Organelle: The Carboxysome Assembly Pathway. *Cell* **155,** 1131–1140 (2013).

4. Detrich, H. W. & Williams, R. C. Reversible dissociation of the alpha beta dimer of tubulin from bovine brain. *Biochemistry* **17,** 3900–7 (1978).

5. Garzón, M. T. *et al.* The dimerization domain of the HIV-1 capsid protein binds a capsid protein-derived peptide: A biophysical characterization. *Protein Sci.* **13,** 1512–1523 (2004).

6. Kodera, N., Yamamoto, D., Ishikawa, R. & Ando, T. Video imaging of walking myosin V by high-speed atomic force microscopy. *Nature* **468,** 72–6 (2010).

7. Preiner, J. *et al.* IgGs are made for walking on bacterial and viral surfaces. *Nat. Commun.* **5,** 4394 (2014).

8. Oshima, H., Hayashi, T. & Kinoshita, M. Statistical Thermodynamics for Actin-Myosin Binding: The Crucial Importance of Hydration Effects. *Biophys. J.* **110,** 2496–2506 (2016).

9. Shibata, M., Yamashita, H., Uchihashi, T., Kandori, H. & Ando, T. High-speed atomic force microscopy shows dynamic molecular processes in photoactivated bacteriorhodopsin. *Nat. Nanotechnol.* **5,** 208–212 (2010).

10. Kitagawa, D. *et al.* Structural basis of the 9-fold symmetry of centrioles. *Cell* **144,** 364–375 (2011).

11. van Breugel, M. *et al.* Structures of SAS-6 suggest its organization in centrioles. *Science (80-.).* **331,** 1196–1199 (2011).

12. Bornens, M. The Centrosome in Cells and Organisms. *Science (80-.).* **335,** 422–426 (2012).

13. Hirono, M. Cartwheel assembly. *Philos Trans R Soc L. B Biol Sci* **369,** (2014).

14. Strnad, P. & Gönczy, P. Mechanisms of procentriole formation. *Trends Cell Biol.* **18,** 389–396 (2008).

15. Pfreundschuh, M., Alsteens, D., Hilbert, M., Steinmetz, M. O. & Müller, D. J. Localizing chemical groups while imaging single native proteins by high-resolution atomic force microscopy. *Nano Lett.* **14,** 2957–2964 (2014).

16. Hilbert, M. *et al.* SAS-6 engineering reveals interdependence between cartwheel and microtubules in determining centriole architecture. **18,** (2016).

17. Rosa-Zeiser, A., Weilandt, E., Hild, S. & Marti, O. The simultaneous measurement of elastic,

electrostatic and adhesive properties by scanning force microscopy: pulsed-force mode operation. *Meas. Sci. Technol.* **8,** 1333–1338 (1997).

18. Ortega-Esteban, A. *et al.* Minimizing tip-sample forces in jumping mode atomic force microscopy in liquid. *Ultramicroscopy* **114,** 56–61 (2012).

19. Xu, X., Carrasco, C., de Pablo, P. J., Gomez-Herrero, J. & Raman, A. Unmasking imaging forces on soft biological samples in liquids when using dynamic atomic force microscopy: a case study on viral capsids. *Biophys. J.* **95,** 2520–8 (2008).

20. Ashby, P. D. Gentle imaging of soft materials in solution with amplitude modulation atomic force microscopy: Q control and thermal noise. *Appl. Phys. Lett.* **91,** (2007).

21. Kumar, B., Pifer, P. M., Giovengo, A. & Legleiter, J. The effect of set point ratio and surface Young's modulus on maximum tapping forces in fluid tapping mode atomic force microscopy. *J. Appl. Phys.* **107,** (2010).

22. Ratcliff, G. C., Erie, D. a. & Superfine, R. Photothermal modulation for oscillating mode atomic force microscopy in solution. *Appl. Phys. Lett.* **72,** 1911–1913 (1998).

23. Nievergelt, A. P., Erickson, B. W., Hosseini, N., Adams, J. D. & Fantner, G. E. Studying biological membranes with extended range high-speed atomic force microscopy. *Sci. Rep.* **5,** 11987 (2015).

24. Johnson, K. L. *Contact Mechanics*. *Cambridge University Press* **108,** (Cambridge University Press, 1985).

25. Guzman, H. V., Perrino, A. P. & Garcia, R. Peak forces in high-resolution imaging of soft matter in liquid. *ACS Nano* **7,** 3198–3204 (2013).

26. Kodera, N., Sakashita, M. & Ando, T. Dynamic proportional-integral-differential controller for high-speed atomic force microscopy. *Rev. Sci. Instrum.* **77,** 83704 (2006).

27. Amo, C. A. & Garcia, R. Fundamental High-Speed Limits in Single-Molecule, Single-Cell, and Nanoscale Force Spectroscopies. *ACS Nano* **10,** 7117–7124 (2016).

28. Ando, T. *et al.* A high-speed atomic force microscope for studying biological macromolecules. *Proc. Natl. Acad. Sci. U. S. A.* **98,** 12468–72 (2001).

29. Schlecker, B. *et al.* Single-cycle-PLL detection for real-time FM-AFM applications. *IEEE Trans. Biomed. Circuits Syst.* **8,** 206–215 (2014).

30. Garcia, R. & Herruzo, E. T. The emergence of multifrequency force microscopy. *Nat. Nanotechnol.* **7,** 217–26 (2012).

31. Martin-Jimenez, D., Chacon, E., Tarazona, P. & Garcia, R. Atomically resolved three-dimensional structures of electrolyte aqueous solutions near a solid surface. *Nat. Commun.* **7,** 12164 (2016).

32. Keller, D. *et al.* Mechanisms of HsSAS-6 assembly promoting centriole formation in human cells. *J. Cell Biol.* **204,** 697–712 (2014).

33. Bauer, M., Cubizolles, F., Schmidt, A. & Nigg, E. A. Quantitative analysis of human centrosome architecture by targeted proteomics and fluorescence imaging. *EMBO J.* **35,** 2152–2166 (2016).

34. Zhang, Y., Zhang, Y. & Marcus, R. B. Thermally actuated microprobes for a new wafer probe card. *J. Microelectromechanical Syst.* **8,** 43–49 (1999).

35. Gönczy, P. Towards a molecular architecture of centriole assembly. *Nat. Rev. Mol. Cell Biol.*
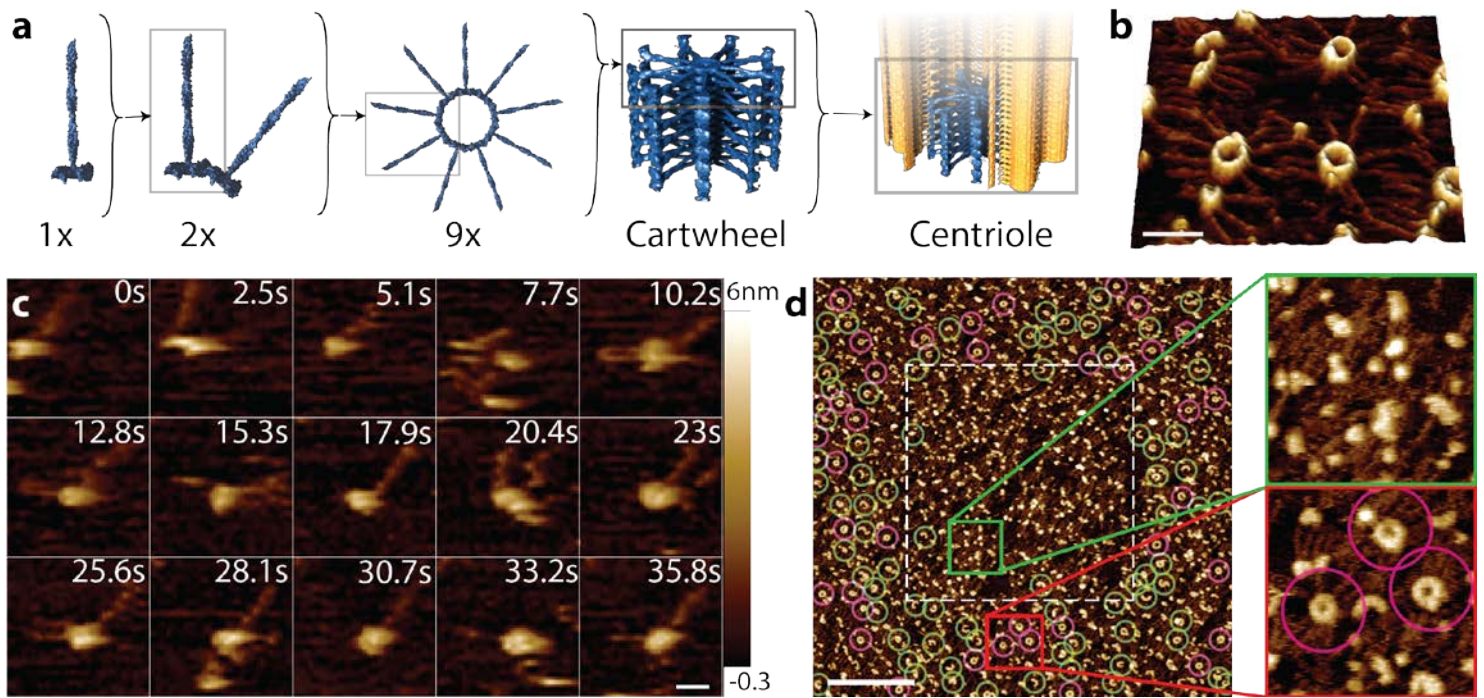
Figure 1: Assembly of the centriolar scaffolding protein CrSAS-6 cannot be observed with conventional high-speed amplitude modulation atomic force microscopy (HS-AM-AFM). a) A single CrSAS-6 homodimer (1x) is composed of a coiled-coil tail and a globular head domain, as well as of un unstructured C terminal region (not represented). CrSAS-6 homodimers interact through their head domains and form intermediates (2x), which eventually assemble into 9-fold symmetric rings (9x) that subsequently stack to form the centriolar cartwheel. The cartwheel (blue) acts as a scaffold for the formation of a new centriole through the recruitment of more peripheral components, including microtubules (yellow). b) High-resolution atomic force microscopy of equilibrated CrSAS-6 assemblies *in vitro* reveal the circular protein ring and the attached spokes (tails). Scale bar is 50nm. c) A HS-AM-AFM frame grabs show SAS-6 homodimers forming intermediate assemblies, which fall apart when scanned multiple times. No formation of full rings can be observed. Scale bar is 10nm, z-scale is 0-6.3nm d) The region imaged with HS-AM-AFM (dashed white square) during assembly is clearly distinct from the surrounding area. Assemblies forming more than half-circles (green rings) and full rings (magenta circles) have been marked and are present essentially only outside of the imaging area (dashed box, where essentially only protein clumps are observed). Scale bar is 300nm, z-scale as in c).
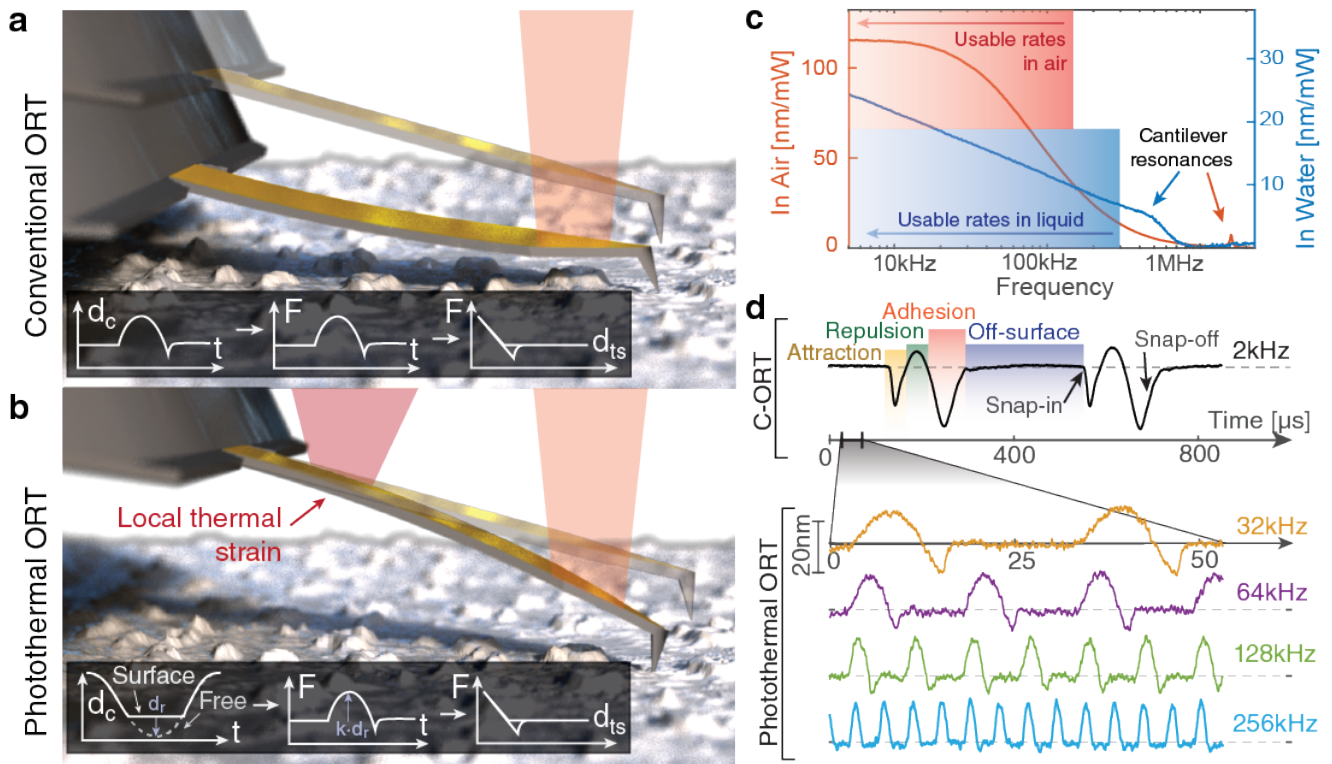
Figure 2: Basic principle of high-speed photothermal off-resonance tapping (HS-PORT). a) Conventional ORT moves the cantilever or the sample to probe the surface with the cantilever tip. The large mass moved in this way by the piezo limits the measurement rate, and in turn the imaging speed. The observed cantilever deflection d_c (inset left) can be directly interpreted as a force (inset middle) and reconstructed into a force distance curve (inset right). b) PORT uses laser based heating to directly actuate the cantilever, ensuring that the mass in motion consists only of the cantilever and the tip. The resulting motion (inset left) is superimposed onto the surface interaction, but the force-time curve (inset middle) can be recovered by subtracting the reference motion, previously recorded away from the surface to get the restricted distance d_r. The force over time is then $k \cdot d_r$ with the spring constant of the cantilever k. A force-distance curve (inset right) can then be reconstructed in the same way as in conventional ORT. c) The photothermal drive response of an 8x2μm high-speed cantilever has a large quasi-static bending region below 300kHz, which is used for ORT actuation. d) The signal observed in ORT has a characteristic heartbeat shape of an adhesive snap-in, a repulsive motion of the cantilever in contact, followed by an adhesive snap-off from the surface (top). In PORT (bottom), the same curves can be reconstructed after subtracting the bending induced by photothermal heating. The reduced mass in motion allows an increase in measurement frequency to 256kHz.
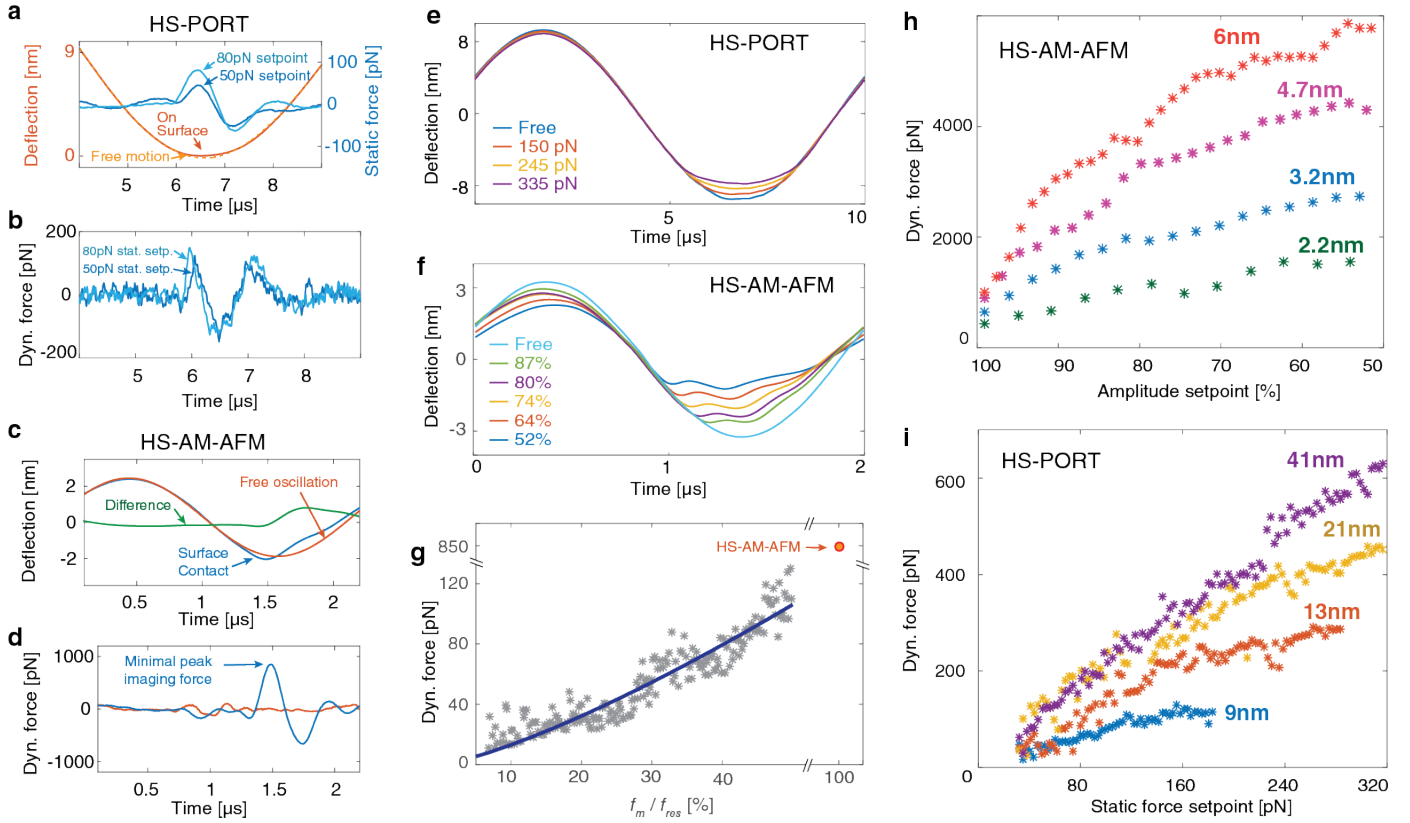
Figure 3: Imaging forces on Mica in liquid, comparing high-speed amplitude modulation AFM (HS-AM-AFM) and high-speed photothermal off-resonance tapping (HS-PORT). a) In HS-PORT (f_m=100kHz), the cantilever actuation is visible in the detector (orange dashed line) and changes upon interacting with the surface (red line). The difference between the two signals is proportional to the static force onto the sample, which is used for topographical feedback. Very small static set point forces (50pN blue, 80pN light blue) can be used. b) Sudden impact of the cantilever onto the surface causes a short dynamic force pulse. This pulse, depending on the amplitude and actuation rate, can surpass the set point force (100pN for static 50pN set point (blue), 160pN for 80pN static set point (light blue)). c) In HS-AM-AFM (f_{res}=505kHz, f_m=480kHz), using a set point reduction of only 0.2nm from a free amplitude of 2nm causes very fast nonlinear impact with the surface (compare blue deflection trace on surface with free motion trace in red, difference in green) followed by an inertia-limited recovery to the steady state amplitude. d) The dynamic impact in HS-AM-AFM causes a short force pulse of 850pN even for a very gentle amplitude set point. e) In PORT, the deflection trace is clipped at the low end, varying with the used set-point. f) In HS-AM-AFM, the impact of the cantilever on the surface causes large clipping of the sinusoidal motion, but only a small change in amplitude shortly before impact. g) The dynamic force in PORT scales approximately with the ratio of measurement frequency to cantilever resonance frequency as $(f_m/f_{res})^{1.3}$ (blue fit). In HS-AM-AFM, this ratio is fixed and the dynamic forces are significantly higher (red circle after axis breaks). h) In HS-AM-AFM, the impact force increases rapidly even at set-points close to the free amplitude. i) In HS-PORT (f_m=100kHz), the dynamic impact force scales gradually with the static force setpoint and increases with larger amplitudes. All cantilever excitation was performed via photothermal drive.
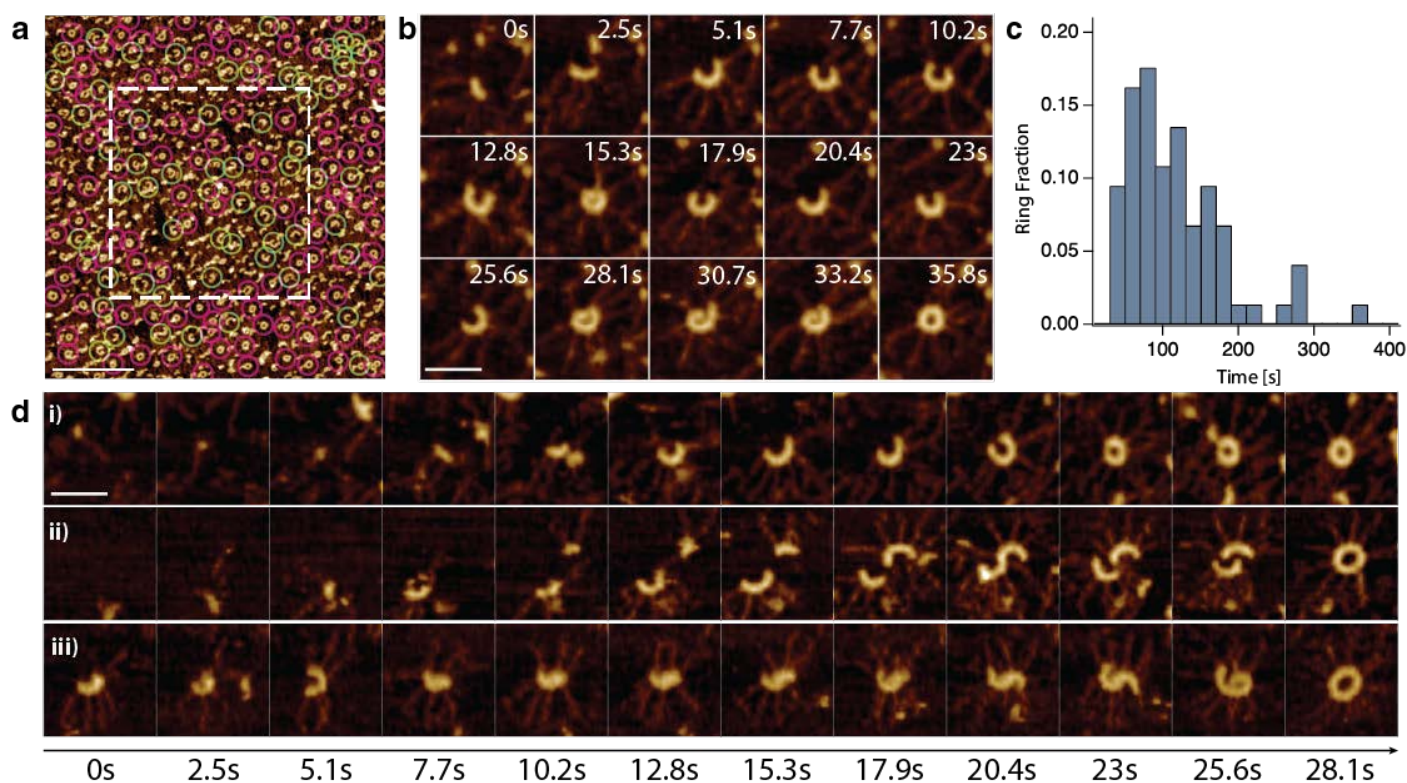
13

Figure 4: Imaging and analysis of CrSAS-6 self-assembly using high-speed photothermal off-resonance tapping (HS-PORT). a) Comparison of the area imaged during assembly (dashed white line) with the surrounding region showing no significant difference in the density of higher-order assemblies (green circles) or full rings (magenta circles). Scale bar is 300nm, z scale is 6.3nm as in fig. 1. b) HS-PORT allows the recording of a full assembly process from the initial stages through a diversity of intermediate assembly stages, ending in a closed ring. Scale bar is 50nm, z-scale is 6.3nm as in Fig.1. c) A histogram of the time from initial nucleation to fully formed CrSAS-6 rings shows an average time of formation of 106 seconds (SD 66), measured over 75 individual assemblies. d) HS-PORT reveals distinct assembly routes. Although rings can be formed by the sequential addition of homodimers (i), the merging of two large fragments can also lead to the formation of a ring (ii). Moreover, in some instances, intermediate metastable states can undergo a conformational change leading to ring formation (iii). Scale bar is 50nm, z range is 0-6.3 nm as in Fig.1.

Methods

Protein expression and purification

The Bld12_NL truncated version of the CrSAS-6/Bld12 protein[10] (58kDa) was expressed in the *E. coli* strain BL21(DE3) (Stratagene). Bacteria were grown at 37 °C to an $OD600_{nm}$ of 0.7 in LB supplied with kanamycin. After induction with 0.5mM IPTG, protein expression was performed ON at 20 °C. Bacterial cells were collected by centrifugation at 4,000g for 10 min (JLA-9.1000, Beckman Coulter). Lysis was achieved by sonication of the resuspended bacterial pellet in 50 mM Tris pH 7.5, 500 mM NaCl supplemented with proteases inhibitors (Complete EDTA-free, Roche). The cellular debris were removed by spinning 1h at 12,000g at 4 °C (JA 25.50, Beckman Coulter). The cleared lysate was then subjected to Ni purification with an HisTrap HP Ni2+-Sepharose columns (GE Healthcare) at 4 °C and further purified by gel-filtration with a HiLoad Superdex 200 16/60 column (GE Healthcare) equilibrated in 20 mM Tris-HCl pH 7.4 supplemented with 150 mM KCl. The sample was concentrated with an Amicon ultra filter with a 10kDa cut-off, aliquoted and stored at -80 °C.

Photothermal off-resonance tapping implementation

Measurement hardware

The HS-AFM consists of a custom built head, scanner and controller (see Figure S6, S7) combined with a commercial piezo amplifier (Techproject, Vienna, Austria), a MultiMode 8 AFM base and a NanoScope 5 controller (both Bruker, Santa Barbara, CA, USA) for sample approach. A spring based vibration isolator (BM4, Minus-K, Inglewood, CA, USA) provides isolation from ambient vibration. The home-built head is compatible with small cantilevers (spot size < 1.5um x 3um) and has a possibility for photothermal drive built in. The head used in this work is an upgraded version from the one we presented previously[36], featuring smaller spot size and improved mechanics. The scanner is a flexure-based high-speed scanner with 1.8um x 1.8um x 2um scan range with ~100 kHz z-Bandwidth that is compatible with the approach mechanism of the MultiMode base (see SI section 3).

Photothermal off-resonance controller

A custom high speed ORT controller consisting of scan engine and off-resonance tapping feedback using photothermal drive was implemented in LabView and LabView FPGA on a PXI system (National Instruments PXIe-1082, Austin, TX, USA) connected to the control computer via an MXI-e interface (PXIe-8370) (see Figures S8-S11). The scan engine runs on an R-series Virtex-5 (PXI-7851R) while the feedback is implemented on a Kintex-7 (PXIe-7975R) with a DC-coupled RF I/O-module (NI 5782). For detailed description of controller implementation please see supplementary information, section 4).

Preparation of SAS-6 samples and AFM imaging

A drop of 50µL of imaging buffer (20 mM TRIS, 150mM KCl, pH 7.4) was injected into the cantilever holder of the head, creating a hanging droplet. The lasers were aligned to the cantilever (BL-AC10DS, Olympus, Tokyo, Japan). Afterwards, the head was placed onto the scanner, directly after cleaving the glued-on 3mm Muscovite Mica disk. Due to heat generated by the readout electronics, the sample temperature is circa 6°C above ambient. The environment was kept at 6-10°C by placing the microscope base, scanner and head into a low-vibration cooler (WL450F-220-FL, Swisscave, Switzerland) to match the temperature which was previously used to assemble SAS-6 rings[37]. The head was turned on and let equilibrate for 15-30 minutes to allow the system to stabilize. The surface was approached in static deflection mode using the NanoScope 5 controller. The piezo was then soft-retracted and the z-piezo control was switched to the home-built controller for PORT imaging or to a digital high-speed lock-in amplifier (UHFLI, Zurich Instruments, Zürich, Switzerland) for HS-AM-AFM.

The concentrated sample was diluted in imaging buffer to a concentration of 175µg/mL. This diluted SAS-6 sample was directly injected to reach a final concentration of 3.5µg/mL. 15µL of imaging buffer were preloaded into the Hamilton syringe to compensate for the dead volume in the liquid cell.

All high-speed scanning shown was performed at 100Hz line rate at 512x256 lines, corresponding to 2.56 seconds/frame. To avoid systematic measurement inaccuracies that might result from spatial or temporal drift of the drive laser, which changes the effective amplitude of the PORT motion, we automatically perform a background correction after each frame.

HS-AM-AFM imaging was done with an amplitude of 1-4nm. The AM-AFM parameters used to obtain the data in figure 1c were 3nm of free amplitude at 500kHz drive by photothermal excitation, a nominal setpoint of 2.6nm (86% of free amplitude) and P an I gain of the controller adjusted as high as possible such that no oscillation occurred. The cantilever had a resonance frequency of 505kHz and a spring constant of k=0.21N/m. PT-ORT was operated at motion amplitudes of 15-50nm with a distance set-point of 350-600pm, corresponding to a force set-point of 70-120pN of static force.

Cantilever tips are e-beam deposited from a carbon precursor onto the existing silicon nitride tips to reduce adhesion of protein to the lever and to reuse the cantilevers.

Force curve measurement and calculation.

Deflection traces for the force calculations in figure 3 were acquired on a freshly cleaved Mica surface (SPI supplies, West Chester, PA, USA) in buffer (Imaging buffer, 20mM TRIS pH 7.4 with 150mM KCl). The use of Mica as a substrate for determining impact forces differences between PORT and HS-AM-AFM allows for a consistent and uniform sample. In the case of a softer substrate, such as CrSAS-

6 proteins, we expect the absolute magnitude of the impact forces to decrease, but the relative difference between the two modes to be conserved.

AM-AFM deflection traces were measured and averaged using the Periodic Waveform Analyser function of the high-speed lock-in amplifier (UHFLI, Zurich Instruments, Zürich, Switzerland). PORT deflection traces were measured and averaged using the home-built PORT controller. To extract the force curves, the second derivative was calculated and multiplied by the effective mass of the cantilever as proposed by Xu *et al.*[19].

Image processing and data analysis

Images were processed in Gwyddion using an in-house developed batch processing script to automatically process large amounts of images. Images were corrected for scanline mismatch (median of differences row alignment) and the background removed (flatten base[38]). For better visibility, a 2-pixel conservative denoising filter and a 0.8 pixel Gaussian filter was applied. Afterwards, the pixels were squared and the images exported in Portable Network Graphics format. Finally, the movies were assembled from individual frames using ffmpeg.

References of methods section

36. Nievergelt, A. P., Adams, J. D., Odermatt, P. D. & Fantner, G. E. High-frequency multimodal atomic force microscopy. *Beilstein J. Nanotechnol.* **5,** 2459–2467 (2014).

37. Guichard, P. *et al.* Cell-free reconstitution reveals centriole cartwheel assembly mechanisms. *Nat. Commun.* **8,** 14813 (2017).

38. Erickson, B. W., Coquoz, S., Adams, J. D., Burns, D. J. & Fantner, G. E. Large-scale analysis of high-speed atomic force microscopy data sets using adaptive image processing. *Beilstein J. Nanotechnol.* **3,** 747–758 (2012).

Data availability statement

The data that support the plots within this paper and other findings of this study are available from the corresponding author upon reasonable request.